Loss of secondary motor cortex neurons in chronic neuropathic pain

Amrita Das Gupta[a,#], Hongwei Zheng[a,#], Livia Asan[a,b], Jennifer John[a], Sanjeev Kaushalya[c,d], Carlo A. Beretta[a,c], Rohini Kuner[c], Johannes Knabbe[a,e], Thomas Kuner[a]

a Department of Functional Neuroanatomy, Institute for Anatomy and Cell Biology, Heidelberg University, Germany.

b Current address: Department of Neurology and Center for Translational Neuro- and Behavioral Sciences (C-TNBS), University Hospital Essen, Germany.

c Department of Molecular Pharmacology, Pharmacology Institute, Heidelberg University, Germany.

d Current address: Cold-Spring-Harbour Laboratory, Neuroscience Center

e Department of General Psychiatry, Centre for Psychosocial Medicine, Heidelberg University, Germany.

# These authors contributed equally.

Correspondence: thomas.kuner@uni-heidelberg.de

Key words: structural plasticity, neuropathic pain, in vivo imaging, tissue composition, neurodegeneration, spine density, dendritic morphology

Abstract

Chronic neuropathic pain is associated with structural plasticity of the brain on different spatial scales, yet, on the mesoscopic scale of tissue composition, little is known. Here, we determined the cellular composition of cortical areas and structural variability of entire neurons during chronic neuropathic pain using longitudinal in vivo two-photon microscopy and behavioral assessment. When monitoring cell type composition in response to spared-nerve injury in 84 cortical volumes containing ~25000 cells each, we found neuronal loss in the secondary motor cortex region M2 immediately adjacent to the cingulate cortex already one week after surgery. Loss of mostly interneurons was also evident when monitoring individual M2 neurons over time. This neuronal loss was preceded by decreased spine density and loss of distal dendritic branches. In conclusion, our work delineates M2 as a novel site and neuronal loss as a so far underappreciated mechanism underlying chronic neuropathic pain states.

Introduction

Chronic neuropathic pain has been shown to be associated with structural alterations of the brain, ranging from macroscopic grey-matter-volume changes (Apkarian et al. 2004; Seminowicz et al. 2009; Bilbao et al. 2018; Silva and Seminowicz 2019) to microscopic alterations on the cellular level (Metz et al. 2009; Kim et al. 2011; Kim and Nabekura 2011; Kassem et al. 2013). In principle, structural neocortical changes associated with chronic pain could be based on a multitude of mechanisms. The most commonly discussed mechanism concerns structural neuronal plasticity, i.e. changes in dendritic architecture and spine density (Holtmaat and Svoboda 2009). Such changes have been shown in many cortical areas to underly functional

45 changes in multifarious physiological and pathophysiological functions such as learning and
46 memory, fear processing, addiction and others (Forrest et al. 2018), and can be viewed as a
47 general disease-relevant mechanism. Changes in the microenvironment of the neuropil
48 including extracellular space regulation (Mascio et al. 2022), ion homeostasis and others could
49 also undergo long-lasting adaptive changes and affect neuronal communication. Such changes
50 would imply astroglial, microglial, oligodendroglial functions and likely also endothelial cells and
51 pericytes. Plasticity could arise from changes in structure and function of these cells, but also by
52 changes in their distribution pattern and number. The latter is well known in neuroinflammation
53 and neurodegeneration, where astrogliosis and proliferation of microglia is particularly well
54 established (Salter and Stevens 2017; Ji et al. 2019). Hence, to address structural mechanisms
55 underlying chronic neuropathic pain states, monitoring the cellular composition of cortical pain
56 areas after induction of chronic pain is a promising avenue to follow. We recently developed an
57 approach called "NuClear" that allows longitudinal, comprehensive, monitoring of cell type-
58 composition in living animals (Das-Gupta et al. 2022). The resulting 3D matrix of identified cells
59 and their location can be repetitively acquired from the identical cortical area and changes in
60 number and location of any cell type can be identified, for example after establishing chronic
61 neuropathic pain using the spared-nerve injury (SNI) model (Decosterd and Woolf 2000).
62 Corresponding changes in pain behavior can be interspersed and allow correlations with
63 structural changes.

64 Cortical pain processing occurs in multiple brain regions also referred to as the pain
65 matrix (Tracey and Mantyh 2007), with each area contributing specialized functions. The
66 cingulate cortex (CC) and its subdivisions is consistently reported to represent emotional and

67 motor aspects of pain perception (Bliss et al. 2016; Kuner and Kuner 2021) and confers pain
68 hypersensitivity via a direct pathway to the posterior insula (Tan et al. 2017). Studies of
69 dendritic structural plasticity have so far addressed the somatosensory (S1) and medial
70 prefrontal cortices (Metz et al. 2009; Kim et al. 2011; Kim and Nabekura 2011), yet has not been
71 studied much in the CC.

72 Here, we attempted to address structural changes of the CC in response to SNI using
73 NuClear and imaging of individual neurons in an in vivo longitudinal study design. In response to
74 SNI, we surprisingly found a loss of neurons in the medial M2 cortex, immediately lateral to the
75 CC. Most of the lost neurons were interneurons, suggesting that loss of inhibition leads to
76 stronger activation of local pyramidal neurons. Neurons prone to die showed a loss of distal
77 dendritic branches and a loss of dendritic spines, suggesting that changes in synaptic inputs
78 may, together with other factors, induce neuronal cell death. In conclusion, we identified medial
79 M2 as a novel player in chronic pain and a loss of M2 neurons as a mechanism previously not
80 considered for chronic pain.

81

82 **Results**

83 We assessed structural changes associated with nerve injury in the cingulate cortex (CC) and
84 adjoining secondary motor cortex (M2) on two levels: (1) changes in tissue composition
85 represented by the number of major brain cell types within large two-photon (2P) imaging
86 volumes (~0.25 mm^3) and (2) cellular and subcellular changes on the level of entire neurons and
87 their dendritic spines (Fig. 1A). Both levels were investigated in a longitudinal paradigm
88 combining SNI, two-photon in vivo imaging and pain behavior (Fig. 1B). Tissue composition was

89 determined by imaging Histon2B-GFP-labelled nuclei (Asan et al. 2021) and subsequent
90 classification of the cell type derived from specific features of the nucleus (Das-Gupta et al.
91 2022)(Das-Gupta et al. 2022). Subcellular changes were investigated by repetitively imaging
92 individually labeled or small groups of labeled neurons in their entirety.
93
94 **SNI reliably induced chronic neuropathic pain states**
95 As a foundation for the structural analysis aimed at by this study, we first report the pain
96 behavioral readouts for both cohorts of mice studied. All mice underwent sensory withdrawal
97 testing using von Frey filaments at the timepoints relative to the SNI or sham surgery as
98 indicated in Figure 1B. Allodynia and hypersensitivity were detected when testing the left hind
99 foot on which surgery was performed (Fig. 1C, Supp. Fig. 1A), but not when testing the right side
100 (Supp. Fig. 1B). Furthermore, cold plate withdrawal was found to be significantly different in
101 SNI-treated mice (Fig. 1D). To test the emotional aspect of pain, we assessed behavior of mice in
102 the open field. SNI-treated mice showed longer lasting immobility, consistent with the presence
103 of a chronic pain state (Fig. 1 E).
104
105 **Tissue composition in volumes encompassing cingulate cortex and adjacent M2 regions**
106 After establishing the development of a chronic pain state in all mice tested, we now focus on
107 cohort 1 mice and tissue composition analysis. We defined four 700 µm x 700 µm x 500 µm
108 large imaging volumes in both hemispheres that were placed as close to the midline as
109 permitted by the sagittal sinus, a structure that obstructs direct 2P imaging of brain areas
110 residing below it (Fig. 2A, Supp. Fig. 2A). Owing to a variable position of large bridging veins

111 towards the sagittal sinus, imaging volumes could not be placed at identical positions in each
112 mouse (indicated by light grey squares in Fig. 2A). We took advantage of this situation by
113 dividing the imaging volumes into cingulate/M2 and M2/M1 volumes, the latter serving as
114 controls for the expected cingulate-specific effects. Nucleus imaging was done before, 1 week
115 and 12 weeks after SNI surgery and yielded 20000 to 30000 cell nuclei per imaging volume (Fig.
116 2B). Using the NuClear approach (Das-Gupta et al. 2022), a method allowing for non-biased
117 neuronal network-based identification of all major cell types residing within the imaging volume
118 solely relying on a set of radiomic features of the cell nucleus (Das-Gupta et al. 2022)we
119 determined 3D matrices of the localization of all neurons, astroglia, oligodendroglia, microglia
120 and endothelial cells present in the volume (Fig. 2C). When applying this analysis to all 84
121 imaging volumes taken from 21 mice, encompassing >2 million cells, no significant changes in
122 cell numbers were found (Fig. 2D). As expected, the most frequent cell type are neurons which
123 were about as abundant as all other cells taken together. When re-slicing the large volumes into
124 coronal sections, the cortical layering becomes evident and the different spatial distributions of
125 the cell types can be appreciated. For example, neurons are organized in layers, microglia and
126 astroglia are evenly distributed at rather constant nearest-neighbor distances (Fig. 2E).
127

128 **Chronic neuropathic pain associated with changes in cell number contralateral to the lesion**

129 We next compared the number of cells in each category at different timepoints post-SNI or
130 sham surgery. Because the medial imaging volumes contain both cingulate cortex and M2 cortex
131 (Fig. 3, center), we digitally separated the volumes into a medial wedge representing the
132 cingulate cortex (black) and a lateral wedge representing the adjoining M2 cortex (light blue).

133 We identified several significant changes in cell number on the contralateral side to the lesion,
134 where such changes are expected to occur (Fig. 3B,D). In contrast, no differences between SNI
135 and sham were detected in ipsilateral volumes (Fig. 3A,C). Hence, we now focus on changes in
136 cell number found for the different cell types on the contralateral side specifically affected by
137 the lesion.
138

139 **Loss of neurons in the medial part of M2 associated with chronic neuropathic pain**

140 A decreased number of neurons was evident already one week after SNI in the medial M2 and
141 the CC (Fig. 3B,D). This decrease persisted throughout week 12 in M2, but not in CC. The weakly
142 significant difference in CC may arise from an imperfect separation of CC versus medial M2
143 regions, with imaging volumes analysed for CC containing a certain fraction of M2 territory. The
144 much stronger and highly significant difference in the number of neurons found in medial M2
145 may thereby 'contaminate' the CC imaging volume. Hence, our data suggests that SNI causes a
146 persistent loss of neurons in the contralateral medial M2 cortex, and to some extent possibly
147 also in the CC. This decrease may contribute to the chronic pain state.
148

149 **Changes in the number of non-neuronal cells**

150 We further found a decrease in the number of astroglia in medial M2 after one week that was,
151 however, no longer evident 12 weeks after the lesion (Fig. 3B). Also microglia show a trend to be
152 decreased in M2. We further detected a significant increase in oligodendroglia in the CC after 12
153 weeks, while the large variability in M2 prevented a similar readout (Fig. 3B). This increase in
154 oligodendrocyte number may suggest an activity-dependent differentiation of oligodendrocyte

155 precursor cells (Faria et al. 2021). Lastly, we found a decrease in endothelial cell number already
156 at week one that persisted until week 12 (Fig. 3B). This may correspond to a reduced capillary
157 density in medial M2 and could go along with a reduced supply of oxygen and nutrients, both of
158 which could be related to neuronal loss.

159 Taken together, our data introduce the medial part of M2 as a new cortical region
160 involved in pain processing and establishes neocortical neuronal cell death as a cellular
161 mechanism underlying chronic neuropathic pain.

162

163 **Longitudinal imaging of individually labeled neurons confirms neuronal loss in medial M2**

164 To validate the findings obtained using the NuClear approach and to learn more about structural
165 changes of individual neurons after SNI surgery, we sparsely labeled neurons within the medial
166 M2 region (Supp. Fig. 3A) and repetitively imaged the same neurons over a time course of 16
167 weeks (see Methods). Figure 4A shows eight labeled and fully reconstructed as well as spatially
168 registered neurons at basal state prior to SNI and at 1, 9 and 16 weeks thereafter. Evidently, only
169 three neurons persist for 16 weeks (N6-8), but already after one week neuron 1 disappeared,
170 followed by neurons 2, 3 and 4 at week 9 (further examples in Supp. Fig 3). On average,
171 approximately 40% of labeled neurons were lost within 16 weeks after SNI (Fig. 4C, red curve).
172 In sharp contrast, nearly all neurons survived over the entire imaging period in sham-treated
173 mice (Fig. 4B, D), indicating that the loss of mGFP expression with time or toxicity triggered by
174 high level mGFP expression over extended time periods are unlikely explanations for neuronal
175 loss. Therefore, we conclude that neurons in the medial M2 region are lost by some mechanism
176 of cell death triggered by SNI.

177

178 **Interneurons are lost more frequently than pyramidal neurons**

179 A differential loss of interneurons versus pyramidal neurons could have a strong impact on
180 network function, with a loss of interneurons reducing local inhibition and thus making
181 pyramidal cells more active, and a loss of pyramidal neurons attenuating the output of the
182 neuronal ensemble in the medial M2. To address this, we sorted the imaged neurons according
183 to morphological parameters into interneurons and pyramidal neurons (see Methods). Our
184 analysis revealed that interneurons are more prone for cell death than pyramidal neurons (Fig.
185 4D). Hence, a more pronounced loss of interneurons predicts a reduction in inhibitory drive
186 within the local M2 network.

187

188 **Structural changes of the dendritic tree precede neuronal loss after SNI**

189 To assess if neurons prone to die undergo some prodromal state of structural changes, we
190 analysed their entire dendritic tree including their postsynaptic spines (see Supp. Fig. 4 for
191 illustration and Methods Supplement for detailed description). For example, neuron 4 (already
192 displayed in Figure 4) underwent a pronounced loss in spine density already within the first
193 week after SNI and barely retained any spines one week later (Figure 5A), to finally disappear
194 before week four. In other neurons we found rearrangements of the dendritic tree. Figure 5B
195 shows neurons 2 and 5 (as in Fig. 4). Each panel shows both neurons at the earlier time point in
196 red and at the later time point in green, hence, structures appearing in yellow exist at both time
197 points while red alone indicates loss of a structure. The pink rectangle marks a dynamic region
198 while the blue rectangle delineates a rather stable region. While dendritic structures are mostly

199 overlapping between basal and day 3 (Fig. 5B1), a loss of distal dendritic branches is evident at
200 week 1 (Fig. 5B2) and progresses further in the delineated area (Fig. 5B3,4). At week 7, neuron 2
201 has disappeared (Fig. 5B5,6). Similar observations were made in all neurons analyzed (Supp. Fig.
202 5). In conclusion, before disappearing, neurons undergo structural changes ranging from a loss
203 of spines to a loss of dendritic branches. These structural changes may reflect alterations in
204 synaptic inputs, possibly triggered by SNI.
205
206 **Discussion**
207 Using NuClear, an unbiased and comprehensive tissue analysis approach, we monitored the
208 cellular composition of the cingulate and M2 cortices after SNI. While monitoring a large tissue
209 volume (in total approximately 21 mm^3) distributed over the medial part of both hemispheres,
210 we found significant changes in cellular composition solely within a small subvolume
211 encompassing the medial part of M2. The most prominent change was a reduction of the
212 number of neurons in medial M2, but also changes in non-neuronal cells, in particular
213 endothelial cells, were observed. The loss of neurons could be validated by longitudinally
214 imaging individually labeled neurons in medial M2. Up to 40% of labelled neurons disappeared,
215 mostly affecting interneurons. Neurons prone to die lost dendritic branches and spines
216 beforehand. In conclusion, our work adds the medial M2 cortex as a novel player in chronic pain
217 processing and suggests selective loss of cortical neurons as a mechanism of chronic pain.
218
219 What is particular about the medial M2?

220 The medial M2 in rodents is considered to belong to the mPFC and is thought to mediate
221 context-dependent and choice-related decisions, to map sensory cues to motor actions, and to
222 potentially also contribute to depressive-like behavior (Barthas and Kwan 2017). Consistent with
223 these diverse functions, this area receives abundant multimodal sensory inputs and projects to
224 sensory, parietal and retrosplenial cortices (Barthas and Kwan 2017). This constellation of
225 functionalities and in particular connectivity makes a role of the medial M2 in pain processing
226 highly plausible, consistent with reports on patients suffering from complex regional pain
227 syndrome (Maihöfner et al. 2007; Jung et al. 2019) However, the detailed connectivity of cells in
228 medial M2 lost after SNI, both in terms of afferent and efferent connections, changes in activity
229 in these projections and their impact on pain behavior await further elucidation.
230
231 A neurodegenerative mechanisms contributing to chronic pain?
232 Our finding of neuronal loss starting as early as one week after SNI suggests that a mechanism
233 of neuronal cell death may get triggered by SNI-induced changes in activity of neurons upstream
234 of M2. The distinct reduction in spine density and loss of distal dendritic branches observed
235 within one week after SNI further supports the idea that the loss of certain synaptic inputs or
236 their altered activity patterns are involved in early steps, thereby eventually resulting in a
237 denervation of distinct M2 neurons. Such loss of afferent input has been reported to result in
238 cell loss (Mostafapour et al. 2000; Inquimbert et al. 2018). Persistent changes in activity, either
239 silence or overactivity, are known to trigger different mechanisms of cell death (Chi et al. 2018;
240 Fricker et al. 2018; Moujalled et al. 2021). Which of these are active in SNI-induced loss of M2
241 neurons remains to be investigated. Alternatively, or synergistically, the neuronal

242 microenvironment defined by glia and endothelial cells might respond to the SNI impact and
243 affect neuron survival. A decreased number of endothelial cells may reflect changes in
244 microvasculature that in turn may negatively affect neuronal fidelity. In conclusion, our work
245 implies neurodegeneration as a mechanism underlying chronic pain states, thereby extending a
246 concept so far limited to the peripheral nervous system (Reichling and Levine 2011) to
247 neocortical circuits.
248
249 How can neuronal loss contribute to the development of a chronic pain state?
250 If neurons get lost, they can no longer contribute to function, yet chronic pain is an active
251 percept generated by as yet unknown interactions of brain areas. As a simple approximation, an
252 increased firing of excitatory M2 output neurons could elicit activity in other areas of the pain
253 matrix and thereby contribute to the pain percept. Likewise, disinhibition via long-range
254 inhibitory connections could achieve the same. Given that we found a more pronounced loss of
255 interneurons within M2, the surviving pyramidal neurons may become more active and thereby
256 contribute to eliciting a pain percept. Interestingly, such local disinhibition in the anterior
257 cingulate network has been described after nerve injury (Blom et al. 2014). Likewise,
258 hyperactive pyramidal neurons in the anterior cingulate have been linked to neuropathic pain
259 (Zhao et al. 2018). In conclusion, while published work supports the mechanisms discussed
260 here, additional work will be needed for a deeper understanding.
261
262 Role of non-neuronal cells

263 In addition to changes in neuronal number we found a consistent change in endothelial cell
264 number. Limited to the medial M2 region, the number of endothelial cells was reduced in SNI-
265 treated mice compared with sham. This effect was already evident at week one and persisted
266 until week 12. At the moment, we can only speculate about the pathophysiological contribution
267 of this change. A possible explanation could be that the microvascular network becomes more
268 sparse after SNI. This could in turn affect the metabolic support of M2 neurons and may be a
269 factor synergistically acting with the structural changes in dendrites and concomitant
270 connectivity. Astroglia were significantly reduced after SNI at week one, but not at week 12. This
271 could be an apparent difference related to the higher variability of the data at week 12.
272 However, the lack of astrogliosis would rather argue against a neurodegenerative mechanism of
273 neuronal cell death in M2 after SNI.
274
275 Technical aspects of our imaging and analysis approach
276 The approach used for comprehensive tissue analysis, NuClear, delivers an unbiased and
277 comprehensive analysis of cell type composition. The number of cell types detected depends on
278 the training data used for the neuronal network and is not limited to the cell types chosen here.
279 The detection accuracy differs between cell types and ranges from 95% for glial cells to 99% for
280 neurons and endothelial cells. By precisely re-identifying imaging volumes acquired at different
281 time points, artificial alterations of cell numbers by misregistration is unlikely to happen.
282 Variations in imaging quality between individual session may in some cases affect the outcome.
283 However, given the large number of volumes analyzed here, such an effect would cancel out

given the study design used here (SNI versus control, volumes ipsi- and contralateral to the lesion, medial versus more lateral volumes).

290 **Materials and Methods**

291

292 Ethical approval

293 The entire study was conducted in line with the European Communities Council Directive
294 (86/609/ECC) to reduce animal pain and/or discomfort. All experiments followed the German
295 animal welfare guidelines specified in the TierSchG. The study has been approved by the local
296 animal care and use council (Regierungspräsidium Karlsruhe, Baden-Wuerttemberg) under the
297 reference numbers G206/11, G294/15 and G27/20. All experiments followed the 3R principle
298 and complied with the ARRIVE guidelines (Percie du Sert, Hurst et al. 2020).

299

300 Animals

301 Transgenic mice expressing the human histone 2B protein (HIST1H2B) fused with enhanced
302 green fluorescence protein (eGFP) under the control of the chicken beta actin promoter (CAG-
303 H2B-eGFP) (Hadjantonakis and Papaioannou 2004) (B6.Cg-Tg(HIST1H2BB/EGFP)1Pa/J, Jackson
304 Laboratory; # 006069) were used in animal experiments of cohort 1 (21 mice in total). C57BL6-J
305 mice were used for cohort 2 (16 mice in total).

306

307 mGFP expression in single neurons (cohort 2)

308 Two adeno-associated virus constructs were used: (1) A DIO cassette containing the synapsin
309 promotor and membrane-bound GFP to achieve long-term neuron-specific expression, (2) a
310 cassette expressing Cre-recombinase under the control of the CBA promotor. The in house-
311 produced AAV1/2 viral particles were stereotaxically injected into the medial M2 region before

312 the cranial window surgery using a high titer of construct (1) and a 10000-20000x dilution of
313 construct (2), both virus solutions were mixed at equal amounts. Stereotaxic coordinates were
314 AP: 1.8 or -0.1 to -0.5, ML: -0.25 to -0.3, DV: – 0.35. This strategy resulted in sufficiently strong
315 expression of mGFP in a few neurons within the target volume.
316
317 Chronic cranial window implantation
318 A craniectomy procedure was performed on each mouse to enable in vivo two-photon imaging
319 following a predefined protocol as described before (Holtmaat, Bonhoeffer et al. 2009). Briefly,
320 the mice were anesthetized with an intraperitoneal injection (i.p.) of a combination of 60 µl
321 Medetomidine (1mg/ml), 160 µl Midazolam (5 mg/ml) and 40 µl Fentanyl (0.05 mg/ml) at a
322 dosage of 3 µl/g body weight. The head was shaved, and the mice were fixed with ear bars in
323 the stereotactic apparatus and eye ointment was applied. Xylocain® 1 % (100 µl, Lidocaine
324 hydrochloride) was applied under the cranial skin and 250 µl Carprofen (0.5 mg/ml) was
325 injected subcutaneously (s.c.). The skin was removed to expose the skull and the surface of the
326 skull was made rough to allow the cement to adhere better. A skull island (approx. 6mm Ø) was
327 drilled centered at bregma using a dental drill and removed with a forceps (#2 FST by Dumont)
328 making sure not to damage the cortical surface. For improved imaging condition, the dura was
329 carefully removed using a fine forceps (#5 FST by Dumont). Normal rat ringer solution (NRR) was
330 applied on the exposed brain surface to keep it moist, and a curved cover glass was placed on
331 top to cover it (Asan, Falfan-Melgoza et al. 2021). With dental acrylic cement (powder: Paladur,
332 Kulzer; activator: Cyano FAST, Hager & Werken GmbH) the cover glass was sealed, and excess
333 cement was used to cover the exposed skull and edges of the skin. A custom designed holder

334 was placed on top of the window and any gaps were filled with cement to ensure maximum
335 adhesion with the skull. After the procedure, the mice were injected (i.p. / s.c.) with a mix of 30
336 µl Atipamezole (5 mg/ml), 30 µl Flumazenil (0.1 mg/m) and 180 µl Naloxon (0.4 mg/ml) at a
337 dosage of 6 µl per gram body weight. To ensure proper recovery of the mice, 3 more doses of
338 Carprofen were given every 8-12 hours and the mice were placed onto a heating plate and
339 monitored.
340
341 In vivo two photon imaging
342 Two photon imaging was carried out with a two-photon microscope (TriM Scope II, LaVision
343 BioTec GmbH) equipped with a tunable pulsed Titanium-Sapphire (Ti:Sa) laser (Chameleon Ultra
344 2; Coherent). Prior to each imaging session, the laser power was adjusted to achieve the best
345 signal to noise ratio. Adaptations were made to minimize the effect of laser attenuation due to
346 tissue depth by creating a z-profile and setting the laser power for different imaging depths
347 while making sure to minimize oversaturation of image pixels.
348
349 In vivo two photon imaging of the H2B-GFP mice (cohort 1)
350 Imaging of H2B-GFP was performed at a laser wavelength of 960 nm. A water immersion
351 objective (16x; NA 0.8, Nikon) was used to obtain volumetric 3D stacks of the H2B-GFP mice.
352 Individual frames consisted of 694 µm x 694 µm in XY with a resolution of 0.29 µm/pixel. Stacks
353 were obtained at varying depths up to 702 µm from the cortical surface with a step size of 2 µm
354 in Z. Mice were initially anesthetized using a vaporizer with 6% isoflurane and eye ointment was
355 applied. For imaging, mice were fixed in a custom-built holder on the microscope stage.

356 Isoflurane (Baxter) was adjusted between 0.5 – 1.5% depending on the breathing rate of each
357 mouse to achieve a stable breathing rate of 55 – 65 breaths per minute with an oxygen flow rate
358 of 0.9 – 1.1 l/min. A heating pad was placed underneath the mouse to regulate body
359 temperature. An infrared camera was used for monitoring of the mice during the imaging.
360

361 In vivo two photon imaging of single cell labelled mice (cohort 2)

362 Imaging of membrane-bound GFP (mGFP) was performed at a laser wavelength of 960 nm. A
363 water immersion objective (25x, NA 1.1, Nikon) was used to obtain overlapping volumetric 3D
364 stacks of whole neurons labelled with mGFP. Individual frames covered an XY area of 292 µm x
365 292 µm, corresponding to a resolution of 143 nm/pixel when sampling at 2048 x 2048 pixels at
366 16 bit gray scale resolution. Using a Z-step size of 1 µm, image stacks consisted typically of 500
367 sections. Four to six adjacent image stacks were acquired with a 15-20% overlap for stitching. A
368 cropped superstack typically consisted of 3600 x 4500 x 500 pixels. Further details are provided
369 in Supplementary Methods.
370 Mice were anesthetized using an intraperitoneal injection (i.p.) of a combination of 60 µl
371 Medetomidine (1mg/ml), 160 µl Midazolam (5 mg/ml) and 40 µl Fentanyl (0.05 mg/ml) at a
372 dosage of 3 µl/g body weight. For imaging, mice were fixed in a custom-built holder on the
373 microscope stage. After the imaging session, mice were injected (i.p. / s.c.) with a mix of 30 µl
374 Atipamezole (5 mg/ml), 30 µl Flumazenil (0.1 mg/m) and 180 µl Naloxon (0.4 mg/ml) at a
375 dosage of 6 µl per gram body weight. For recovery, mice were kept on a heating plate.
376

377 SNI surgery

378 For the induction of neuropathic pain, a spared nerve injury (SNI) of the sciatic nerve was
379 performed after baseline imaging as described elsewhere (Gangadharan et al. 2022). Briefly,
380 mice were anesthetized using isoflurane as described above. After applying a local anesthetic,
381 an incision on the left hindpaw was made above the sciatic nerve. The peroneal and tibial nerve
382 were ligated and cut and the sural nerve (innervating the lateral part of the ipsilateral paw) was
383 left intact.
384
385 Behavior analysis
386 For habituation, mice were placed in the dark behavior room for 3 days, one hour each prior to
387 the day of the experiment as well as the day of the experiment. All behavior experiments were
388 performed in the dark cycle of the circadian rhythm of the mice under red light conditions.
389
390 von Frey test
391 To test hypersensitivity after chronic pain induction, the von Frey test was used as described
392 elsewhere (Gangadharan et al. 2022). Briefly, all mice were habituated on the von Frey grid
393 prior to the experiment. Each mouse was stimulated on the lateral part of both the ipsilateral
394 and contralateral paw with von Frey filaments ranging from 0.07 g to 1.4 g. Each filament test
395 consisted of 5 trials and trials were either marked 0 (negative response) or 1 (positive response)
396 depending on whether the mouse showed any response like paw flicking, licking or flinching
397 behavior. For analysis, a mouse was classified as being responsive to a certain filament when
398 more than 50% of the trials were positive.
399

400 Cold plate test

401 To test allodynia, the cold plate test way used (Tan et al. 2017). The cold plate was set at 4°C
402 and mice were lowered onto the plate and the latency for a reaction was tested for 30s. The
403 time for a first aversive response (paw withdrawal, jumping, licking) was noted and any mouse
404 not responding during the first 30 s was assigned a latency of 30 s.

405

406 Open field test

407 The open field test was used to test for the emotional aspect of pain. The setup consists of a
408 50cm x 50cm box with 15 cm high walls and a separate distinction for the center of the box.
409 Mice were placed in the center of the box and were subsequently recorded with a video
410 camera for 5 minutes. A custom script was designed in Bonsai for mouse tracking and analysis
411 of time spent in the center or outside the center of the box. Immobility time excluding
412 grooming was manually scored by an investigator blinded for the mice.

413

414 Reidentification of stack positions over time in cohort 1

415 To be able to compare cell type changes in the same volume over time, the imaging positions of
416 each imaging volume had to be identical. To achieve this, three or more large vessels on the
417 cortical surface were used as fiducials. The center of the first vessel was set as zero on both X
418 and Y coordinates of the microscope stage. The coordinates of the subsequent vessels and
419 stacks were noted with respect to the first vessel. For imaging of the subsequent timepoint, the
420 coordinates were used to identify the approximate location of the stack. After roughly
421 reidentifying the imaging position, the microscopi field of view in different imaging planes along

422 the Z-axis was aligned to fit to the previous position. A registration system based on the
423 distance and angle of the first vessel from bregma was created using a self-written script in
424 Python, which was used to assign the position of all imaging volumes with respect to bregma.
425 Using a mouse brain atlas (Paxinos & Franklin, 2012), imaging volumes were selected which
426 were located in the secondary motor area (M2) and the cingulate cortex (CC). Each imaging
427 volume was divided into diagonal wedges (Fig. 3) corresponding the M2 and CC regions for both
428 ipsilateral and contralateral hemispheres for further analysis. Due to a "pseudo"-dura consisting
429 of probably fibroblasts growing on top of the brain, imaging was started from ~76 µm below
430 occurrence of the first fluorescent signal. Imaging was performed until 550 µm below the first
431 fluorescent signal due signal-to-noise ratio increasing with depth.
432
433 Image analysis of individual neurons used in cohort 2
434 The image analysis pipeline is illustrated in Supp. Figure 4 and described in detail in the
435 Methods supplement.
436 Morphometric sorting of neurons
437 Interneurons were identified based on their multipoloar shape, lower spine density and small
438 size. Pyramidal neurons were identified by the typical pyramidal shape of the soma and a strong
439 apical dendrite, high spine density, and large size.
440
441 Antibody staining
442 Antibody staining was performed on 50 µm thick brain slices with following antibodies: Anti-
443 NeuN (monoclonal mouse) antibody (Synaptic Systems; #266 011; dilution 1:500), Anti-IBA1

444 (polyclonal rabbit) antibody (Fujifilm – Cellular dynamics; #019-19741; dilution 1:250), Anti-
445 S100ß (polyclonal chicken) antibody (Synaptic Systems; #287 006; dilution 1:500) for astroglia.
446 Secondary antibodies were used with 1:500 dilution.
447
448 NuClear analysis for identification of cell types belonging to individual H2B nuclei
449 Details of this method are published elsewhere (Das-Gupta et al. 2022). Briefly, automated
450 segmentation of all nuclei was performed with the StarDist neuronal network using a high
451 performance cluster environment (bwForCluster MLS&WISO). Afterwards, radiomics features
452 for every segmented nucleus were extracted using the PyRadiomics library and self-written
453 python scripts. Every segmented nucleus was classified with five pre-trained neuronal network
454 classifiers and assigned a unique class (neurons, astroglia, microglia, oligodendroglia,
455 endothelial cells). Nuclei that were assigned to two or more classes were assigned to the
456 "undecided" class; nuclei that were assigned to no class were labelled as "unclassified".
457
458 Statistical analysis
459 In general, statistical analysis was performed in R (R. Core Team 2021). Depending on the
460 distribution of the data either t-tests or non-parametric statistical test (Wilcoxon signed-rank
461 test) were used for statistical testing, p-values were corrected for multiple comparisons using
462 the "Bonferroni"-method. Plots were created using the R package "ggplot2" (Wickham 2016).
463
464 Statistical analysis of 3D cell type distribution

All data were stored in a local MySQL database (MySQL Workbench 8.0). Data were imported into R. Cell count and first nearest neighbor distance were calculated for each cell type for different timepoints. The nearest neighbor distance was calculated using the "spatstat" package for R (Baddeley and Turner 2005).

Contributions

ADG: Cohort 1. Cranial window and SNI surgeries, imaging data acquisition, implementation and development of analysis pipeline, data analysis, conceptual inputs, generation of figures.

HZ: Cohort 2. Analysis of 2P in vivo imaging data, development of automated tracing algorithm compatible with large data volumes, generation of figures.

JJ: Cohort 1. Cranial window and SNI surgeries, behavior and imaging data acquisition, tissue volume reidentification.

LA: Cohort 1. Development of the initial analysis pipeline for nucleus-based cell type identification, tissue volume reidentification script.

CAB: Cohort 1. Development of segmentation, application of StarDist.

SK: Cohort 2: Cranial window implantations, SNI surgeries and 2P imaging data acquisition.

RK: Initial conceptual input.

JK: Conceptualization, implementation, experimentation, analysis, writing of the MS, project management and supervision.

TK: Project idea and concept, writing of the MS, supervision.

Acknowledgements

We want to thank Michaela Kaiser, Dunja Baumgartl-Ahlert and Nadine Gehrig for their excellent technical support during preparation and execution of experiments. We thank Deepitha Männich for help with posthoc analysis. We gratefully acknowledge the support by the German Research Foundation (DFG) (SFB1158, project B08 awarded to TK), the data storage service SDS@hd, supported by the Ministry of Science, Research and the Arts Baden-Württemberg (MWK) and the DFG through grant INST 35/1314-1 FUGG, as well as the high performance cluster bwForCluster MLS&WISO and HELIX, supported by the MWK and the DFG through Grant INST 35/1134-1 FUGG.

498 **Figure legends**

499

500 **Figure 1: Experimental design (a)** A spared nerve injury (SNI) surgery was carried to induce
501 chronic pain in mice. Effects of SNI were studied in the secondary motor area (M2) and anterior
502 cingulate cortex (ACC) using in vivo 2-photon (2P) microscopy of cell nuclei and single neurons.
503 Nuclei were classified into cell types using a neural network classifier. (**b)** Longitudinal study
504 design for Cohort 1 (nuclei imaging) and cohort 2 (single neuron imaging) **(c)** von Frey test
505 shows significant differences of the threshold filament between sham and SNI animals at 50%
506 paw withdrawal threshold and **(d)** cold plate latency is significantly lower in SNI mice. **(e)**
507 Immobility time showing significant difference between SNI and Sham. All behavior data N=10
508 for SNI and sham.

509

510 **Figure 2: Imaging analysis of cohort 1 (a)** Schematic representation of imaging areas for 2P
511 imaging in cohort 1 **(b)** 3D reconstruction of a volumetric image. Zoom in shows a sub volume
512 and a 2D maximum intensity projection (50 µm). **(c)** Imaging positions were reidentified over
513 time using large vessels as fiducials. Each imaging volume was further classified into different
514 cell types using a pre-trained neuronal network. **(d)** Absolute cell count per mm^3 for different
515 imaging timepoints. N=10 for SNI and sham. **(e)** Coronal projections (700 µm and 100 µm)
516 showing distribution of classified cells in distinct pattens.

517

518 **Figure 3: Changes in cell type composition in CC and M2 (a)** Cell type changes in ipsilateral and
519 contralateral hemispheres. Inlay depicts a schematic representation of the imaging volumes

520 with regard to brain areas (dotted line), ACC nuclei are shown in blue, M2 nuclei in black. N left
521 panel: SNI =7 / Sham = 10; right panel: SNI = 9 / Sham = 7. Wilcox test. M2: week 1 contralateral
522 neurons: *** (p = 0.000175); Aglia: ** (p = 0.005240); EC: * (p = 0.022900); week 12:
523 contralateral neurons : * (p = 0.03110); EC = ** (p = 0.00122). CC: Week 1 contralateral neurons
524 : * (p = 0.0311); Week 12 contralateral Olig: * (p = 0.0418).
525
526 **Figure 4: Loss of cells in medial M2 after SNI.** (a) A group of eight M2 neurons imaged before
527 SNI (basal) and 1, 9 and 12 weeks after SNI. Images show cells after image processing as
528 summarized in Supp. Fig. 4 and the Methods supplement. Shown are fully reconstructed
529 neurons with the raw fluorescence excised based on the traced skeleton (hence no background
530 visible). Scale bar 100 µm. (b) Neuron imaged in M2 of a sham mouse at the same time points
531 reported in (a). Scale bar 100 µm. (c) Quantitative comparison of the number of cells counted at
532 different time points in sham and SNI treated mice. N=20 cells for sham and N=28 for SNI, taken
533 from a total of 16 mice. Mean ± SEM. ANOVA with Bonferoni multiple comparison test, * depict
534 P <0.05. (d) Quantitative comparison of the number of lost interneurons versus pyramidal
535 neurons after SNI. N=14 pyramidal cells and N=18 interneurons, taken from a total of 16 mice.
536 Mean ± SEM. ANOVA with Bonferoni multiple comparison test, * depict P <0.05.
537
538 **Figure 5: Spine loss and changes in dendritic morphology.** (a) Neuron 4 (from Fig. 4) imaged at
539 basal state, 3 days, 1 week and 2 weeks after SNI. Neuron disappeared before week 4. Scale bar
540 20 µm. (b) Neurons 2 and 5 (from Fig. 4) imaged at multiple time points as indicated. The
541 respectively earlier time point is shown in red, the later time point in green, so that preserved

542 cellular morphology will display yellow, but lost structures appear in red. The two colour-coded
543 insets (scale bars 20 µm) show details of a dynamic region (magenta) and a static region (blue).
544 Scale bar in upper panels = 50 µm.
545
546 **Supplementary Figure 1: Sensory testing of cohort 2 mice.** Von Frey withdrawal thresholds for
547 SNI (N=7) and sham mice (N=6). Mean ± SEM.
548
549 **Supplementary Figure 2: Scheme illustrating the imaging situation at the cingulate cortex.** The
550 red square represents the imaging volume of 700 µm width. The triangle demarks the sagittal
551 sinus. Drawing approximately to scale. AP position of coronal section at approximately -0.2. M1
552 primary motor cortex, M2 secondary motor cortex, Cgd dorsal cingulate cortex, Cgv ventral
553 cingulate cortex.
554
555 **Supplementary Figure 3: Post-hoc analysis of neurons located in the medial M2.** Two examples
556 (A1, A2) of neurons stained with anti-GFP antibody in fixed coronal sections. Parvalbumin
557 staining (red). Triangles represent the medial M2 region. Scale bar 200 µm.
558
559 **Supplementary Figure 4: Illustration of image analysis pipeline.** (a) Panels showing different
560 steps in image processing. (a1) raw data. (a2) data excised from (a1) using the traced skeleton
561 (a3). (b) Workflow of Bayesian learning-based iterative image analysis strategy. A detailed
562 description can be found in the Supplemental Methods.
563

564 **Supplementary Figure 5: Changes in spine density in neurons prone to die.** Comparison of
565 spine density determined for entire neurons over time. Neurons imaged in sham mice (black),
566 neurons imaged in SNI mice surviving 16 weeks, and neurons surviving four weeks or less (blue).
567 Mean ± SEM, N=4 mice in each group, ANOVA with Bonferroni multiple comparison (* = $P <$
568 0.05).
569
570

571 **References**

572

573 Apkarian AV, Sosa Y, Sonty S, et al (2004) Chronic back pain is associated with decreased
574 prefrontal and thalamic gray matter density. The Journal of neuroscience: the official
575 journal of the Society for Neuroscience 24:10410–10415.
576 https://doi.org/10.1523/jneurosci.2541-04.2004

577 Asan L, Falfán-Melgoza C, Beretta CA, et al (2021) Cellular correlates of gray matter volume
578 changes in magnetic resonance morphometry identified by two-photon microscopy.
579 Scientific Reports 11:4234. https://doi.org/10.1038/s41598-021-83491-8

580 Barthas F, Kwan AC (2017) Secondary Motor Cortex: Where 'Sensory' Meets 'Motor' in the
581 Rodent Frontal Cortex. Trends Neurosci 40:181–193.
582 https://doi.org/10.1016/j.tins.2016.11.006

583 Bilbao A, Falfán-Melgoza C, Leixner S, et al (2018) Longitudinal Structural and Functional Brain
584 Network Alterations in a Mouse Model of Neuropathic Pain. Neuroscience 387:104–115.
585 https://doi.org/10.1016/j.neuroscience.2018.04.020

586 Bliss TVP, Collingridge GL, Kaang B-K, Zhuo M (2016) Synaptic plasticity in the anterior cingulate
587 cortex in acute and chronic pain. Nat Rev Neurosci 17:485–96.
588 https://doi.org/10.1038/nrn.2016.68

589 Blom SM, Pfister JP, Santello M, et al (2014) Nerve Injury-Induced Neuropathic Pain Causes
590 Disinhibition of the Anterior Cingulate Cortex. Journal of Neuroscience 34:5754–5764.
591 https://doi.org/10.1523/jneurosci.3667-13.2014

592 Chi H, Chang H-Y, Sang T-K (2018) Neuronal Cell Death Mechanisms in Major
593 Neurodegenerative Diseases. Int J Mol Sci 19:3082. https://doi.org/10.3390/ijms19103082

594 Das-Gupta A, Asan L, John J, et al (2022) Comprehensive monitoring of tissue composition using
595 in vivo imaging of cell nuclei and deep learning. Biorxiv 2022.10.03.510670.
596 https://doi.org/10.1101/2022.10.03.510670

597 Decosterd I, Woolf CJ (2000) Spared nerve injury: an animal model of persistent peripheral
598 neuropathic pain. Pain 87:149–158. https://doi.org/10.1016/s0304-3959(00)00276-1

599 Faria O de, Pivonkova H, Varga B, et al (2021) Periods of synchronized myelin changes shape
600 brain function and plasticity. Nat Neurosci 24:1508–1521. https://doi.org/10.1038/s41593-
601 021-00917-2

602 Forrest MP, Parnell E, Penzes P (2018) Dendritic structural plasticity and neuropsychiatric
603 disease. Nat Rev Neurosci 19:215–234. https://doi.org/10.1038/nrn.2018.16

604 Fricker M, Tolkovsky AM, Borutaite V, et al (2018) Neuronal Cell Death. Physiol Rev 98:813–880.
605 https://doi.org/10.1152/physrev.00011.2017

606 Gangadharan V, Zheng H, Taberner FJ, et al (2022) Neuropathic pain caused by miswiring and
607 abnormal end organ targeting. Nature 1–9. https://doi.org/10.1038/s41586-022-04777-z

608 Holtmaat A, Svoboda K (2009) Experience-dependent structural synaptic plasticity in the
609 mammalian brain. Nature Reviews Neuroscience 10:647–658.
610 https://doi.org/10.1038/nrn2699

611 Inquimbert P, Moll M, Latremoliere A, et al (2018) NMDA Receptor Activation Underlies the
612 Loss of Spinal Dorsal Horn Neurons and the Transition to Persistent Pain after Peripheral
613 Nerve Injury. Cell Reports 23:2678–2689. https://doi.org/10.1016/j.celrep.2018.04.107

614 Ji R-R, Donnelly CR, Nedergaard M (2019) Astrocytes in chronic pain and itch. Nature Reviews
615 Neuroscience 20:667–685. https://doi.org/10.1038/s41583-019-0218-1

616 Jung H-Y, Kim J-H, Lee WJ, et al (2019) Microstructural Abnormalities of the Secondary Motor
617 Area Coordinating Sensory and Motor Functions in Patients with Complex Regional Pain
618 Syndrome. Neuropsychiatry 9:2419–2427

619 Kassem MS, Lagopoulos J, Stait-Gardner T, et al (2013) Stress-induced grey matter loss
620 determined by MRI is primarily due to loss of dendrites and their synapses. Molecular
621 neurobiology 47:645–661. https://doi.org/10.1007/s12035-012-8365-7

622 Kim S, Kato G, Ishikawa T, Nabekura J (2011) Phase-specific plasticity of synaptic structures in
623 the somatosensory cortex of living mice during neuropathic pain. Molecular Pain 7:87.
624 https://doi.org/10.1186/1744-8069-7-87

625 Kim SK, Nabekura J (2011) Rapid synaptic remodeling in the adult somatosensory cortex
626 following peripheral nerve injury and its association with neuropathic pain. 31:5477–5482.
627 https://doi.org/10.1523/jneurosci.0328-11.2011

628 Kuner R, Kuner T (2021) Cellular Circuits in the Brain and Their Modulation in Acute and Chronic
629 Pain. Physiol Rev 101:213–258. https://doi.org/10.1152/physrev.00040.2019

630 Maihöfner C, Baron R, DeCol R, et al (2007) The motor system shows adaptive changes in
631 complex regional pain syndrome. Brain 130:2671–2687.
632 https://doi.org/10.1093/brain/awm131

633 Mascio G, Notartomaso S, Martinello K, et al (2022) A Progressive Build-up of Perineuronal Nets
634 in the Somatosensory Cortex Is Associated with the Development of Chronic Pain in Mice. J
635 Neurosci 42:3037–3048. https://doi.org/10.1523/jneurosci.1714-21.2022

636 Metz AE, Yau H-J, Centeno MV, et al (2009) Morphological and functional reorganization of rat
637 medial prefrontal cortex in neuropathic pain. Proceedings of the Royal Society of London
638 Series B, Containing papers of a Biological character Royal Society (Great Britain) 106:2423–
639 2428. https://doi.org/10.1073/pnas.0809897106

640 Mostafapour SP, Cochran SL, Puerto NMD, Rubel EW (2000) Patterns of cell death in mouse
641 anteroventral cochlear nucleus neurons after unilateral cochlea removal. J Comp Neurol
642 426:561–571. https://doi.org/10.1002/1096-9861(20001030)426:4<561::aid-cne5>3.0.co;2-
643 g

644 Moujalled D, Strasser A, Liddell JR (2021) Molecular mechanisms of cell death in neurological
645 diseases. Cell Death Differ 28:2029–2044. https://doi.org/10.1038/s41418-021-00814-y

646 Reichling DB, Levine JD (2011) Pain and death: Neurodegenerative disease mechanisms in the
647 nociceptor. Ann Neurol 69:13–21. https://doi.org/10.1002/ana.22351

648 Salter MW, Stevens B (2017) Microglia emerge as central players in brain disease. Nat Med
649 23:1018–1027. https://doi.org/10.1038/nm.4397

650 Seminowicz DA, Laferriere AL, Millecamps M, et al (2009) MRI structural brain changes
651 associated with sensory and emotional function in a rat model of long-term neuropathic
652 pain. NeuroImage 47:1007–1014. https://doi.org/10.1016/j.neuroimage.2009.05.068

653 Silva JTD, Seminowicz DA (2019) Neuroimaging of pain in animal models: a review of recent
654 literature. Pain Reports 4:e732. https://doi.org/10.1097/pr9.0000000000000732

655 Tan LL, Pelzer P, Heinl C, et al (2017) A pathway from midcingulate cortex to posterior insula
656 gates nociceptive hypersensitivity. Nat Neurosci 20:1591–1601.
657 https://doi.org/10.1038/nn.4645

658 Tracey I, Mantyh PW (2007) The Cerebral Signature for Pain Perception and Its Modulation.
659 Neuron 55:377–391. https://doi.org/10.1016/j.neuron.2007.07.012

660 Zhao R, Zhou H, Huang L, et al (2018) Neuropathic Pain Causes Pyramidal Neuronal
661 Hyperactivity in the Anterior Cingulate Cortex. Front Cell Neurosci 12:107.
662 https://doi.org/10.3389/fncel.2018.00107

663

Figure 1

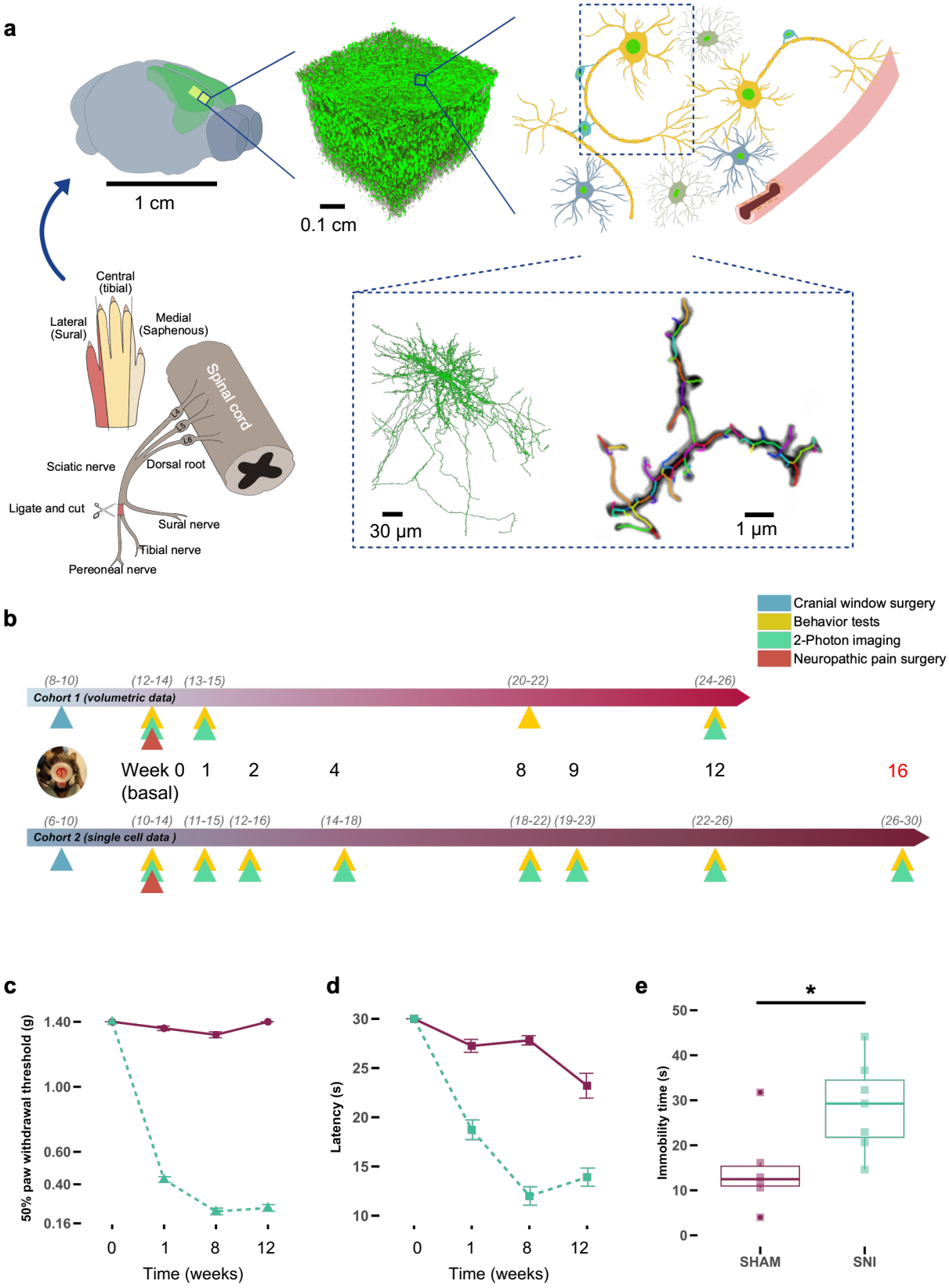
a
1 cm
0.1 cm
Central (tibial)
Lateral (Sural)
Medial (Saphenous)
Spinal cord
L4
L5
L6
Sciatic nerve
Dorsal root
Ligate and cut
Sural nerve
Tibial nerve
Pereoneal nerve
30 µm
1 µm
b
Cranial window surgery
Behavior tests
2-Photon imaging
Neuropathic pain surgery
(8-10)
(12-14)
(13-15)
(20-22)
(24-26)
Cohort 1 (volumetric data)
Week 0 (basal)
1
2
4
8
9
12
16
(6-10)
(10-14)
(11-15)
(12-16)
(14-18)
(18-22)
(19-23)
(22-26)
(26-30)
Cohort 2 (single cell data)
c
50% paw withdrawal threshold (g)
1.40
1.00
0.60
0.40
0.16
0
1
8
12
Time (weeks)
d
Latency (s)
30
25
20
15
10
0
1
8
12
Time (weeks)
e
*
Immobility time (s)
50
40
30
20
10
0
SHAM
SNI

Figure 2

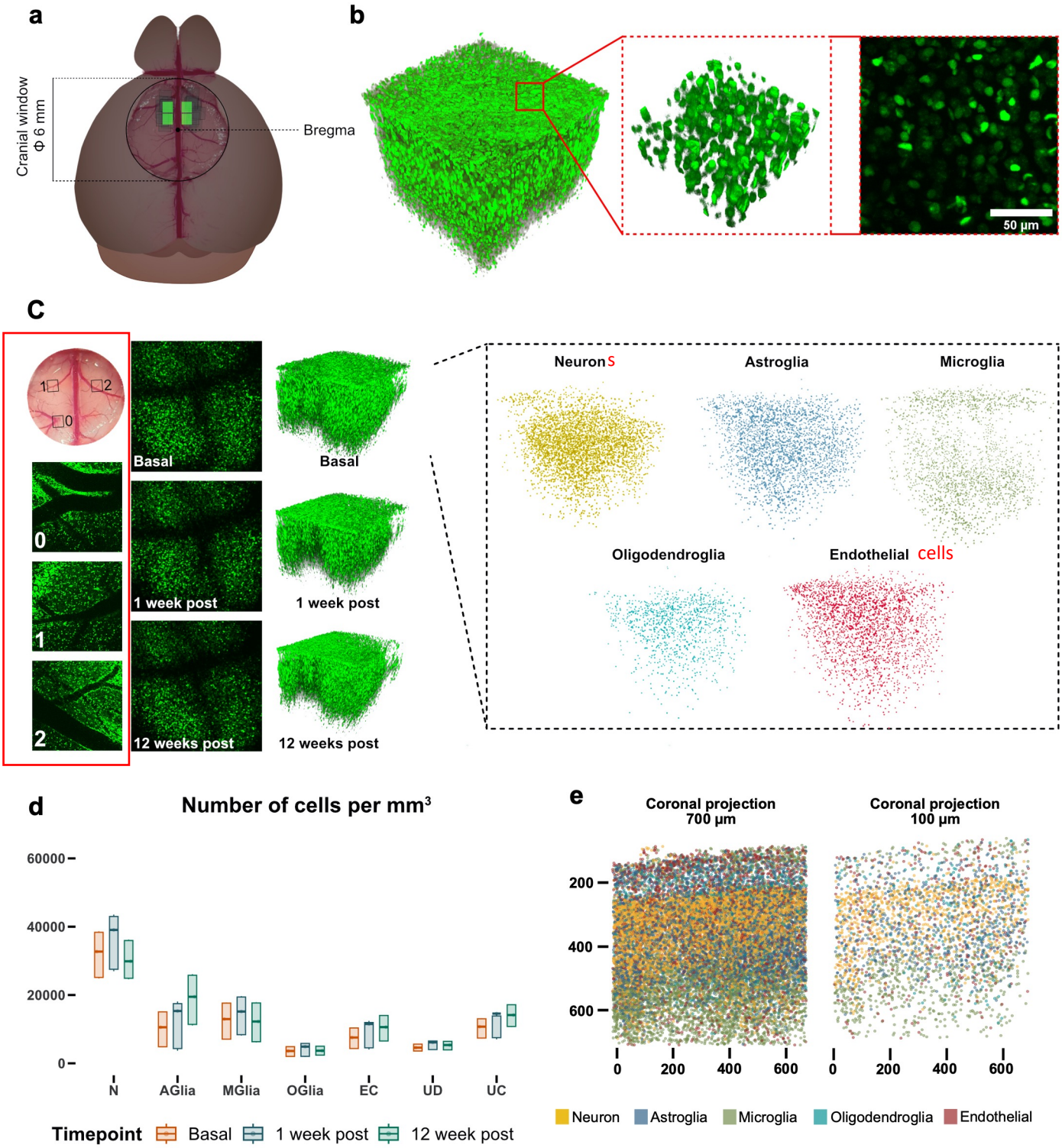
a
Cranial window
Φ 6 mm
Bregma
b
50 µm
c
1
2
0
Basal
1 week post
12 weeks post
Neurons
Astroglia
Microglia
Oligodendroglia
Endothelial cells
d
Number of cells per mm³
60000
40000
20000
0
N
AGlia
MGlia
OGlia
EC
UD
UC
Timepoint
Basal
1 week post
12 week post
e
Coronal projection
700 µm
Coronal projection
100 µm
200
400
600
0
Neuron
Astroglia
Microglia
Oligodendroglia
Endothelial

Figure 3

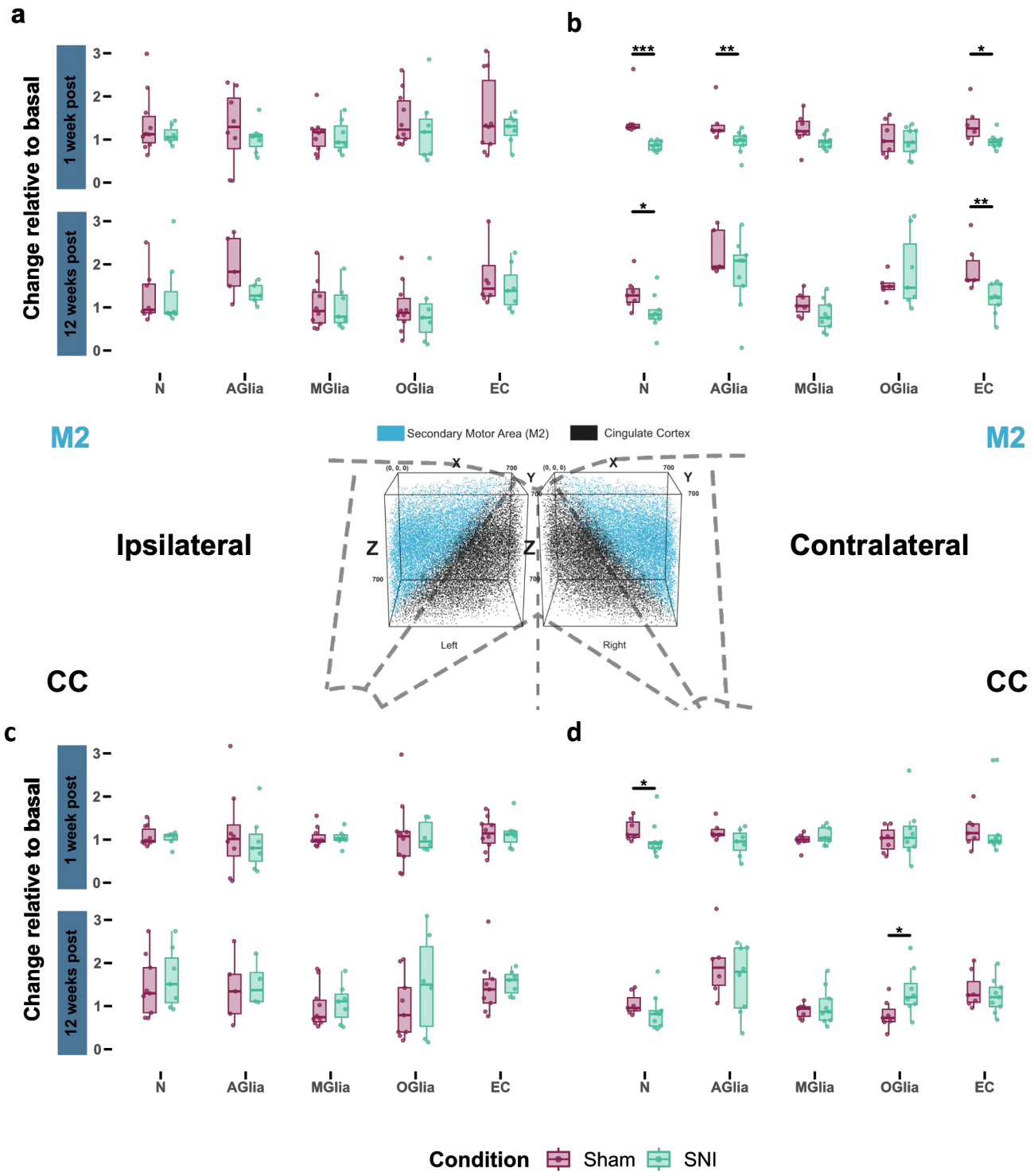
a
b
c
d
Change relative to basal
1 week post
12 weeks post
N
AGlia
MGlia
OGlia
EC
M2
M2
Secondary Motor Area (M2)
Cingulate Cortex
Ipsilateral
Contralateral
CC
CC
Left
Right
Condition
Sham
SNI

Figure 4

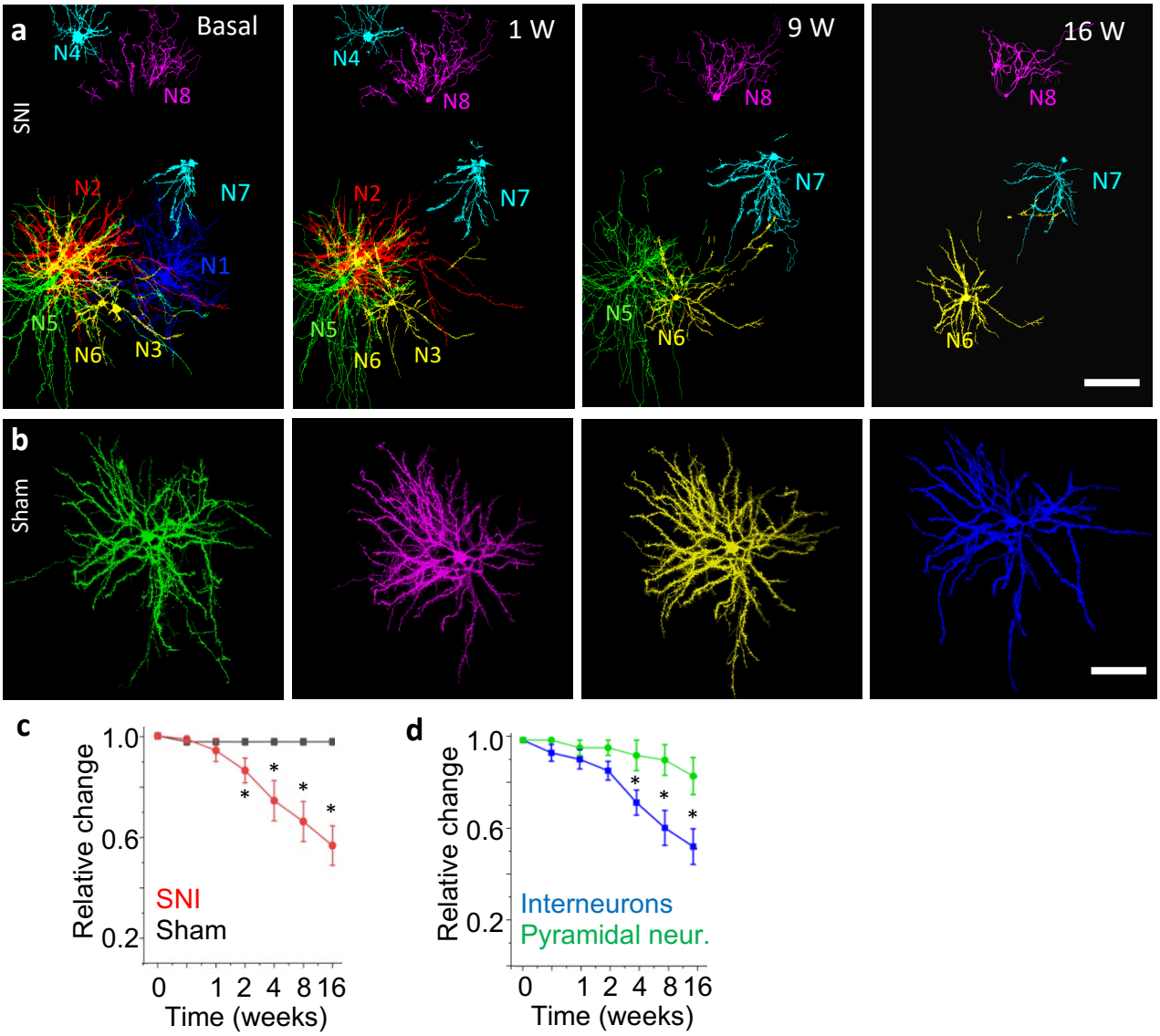
a
Basal
1 W
9 W
16 W
SNI
N4
N8
N2
N7
N1
N5
N6
N3
b
Sham
c
Relative change
1.0
0.6
0.2
SNI
Sham
0
1
2
4
8
16
Time (weeks)
d
Relative change
1.0
0.6
0.2
Interneurons
Pyramidal neur.
0
1
2
4
8
16
Time (weeks)

Figure 5

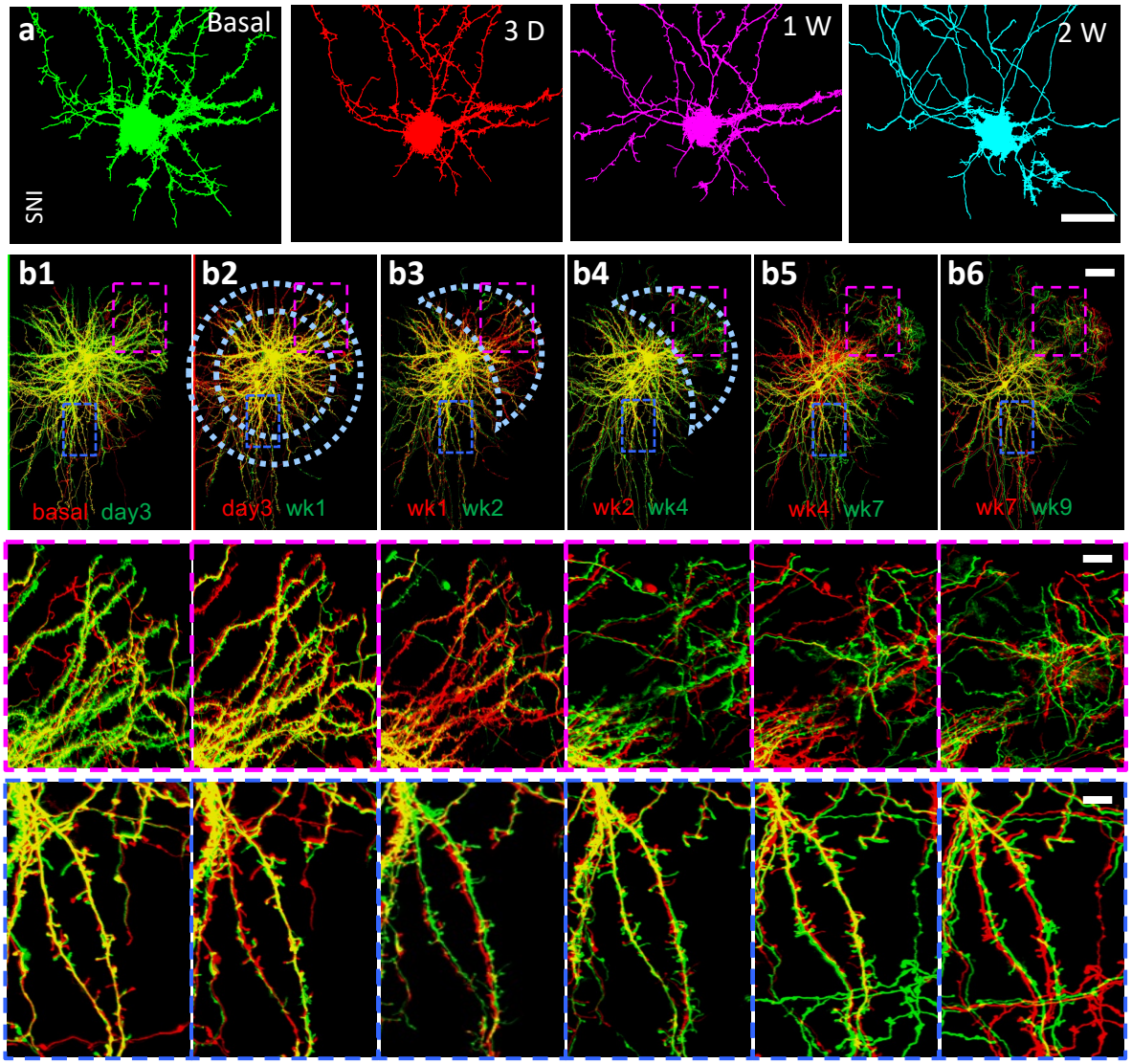
a
Basal
SNI
3 D
1 W
2 W
b1
b2
b3
b4
b5
b6
basal day3
day3 wk1
wk1 wk2
wk2 wk4
wk4 wk7
wk7 wk9

Supplementary Figure 1

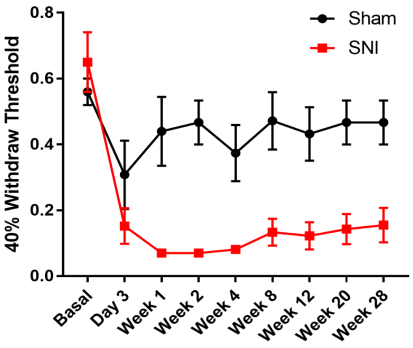

Supplementary Figure 2

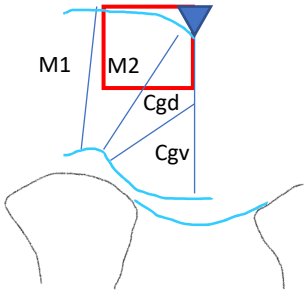

Supplementary Figure 3

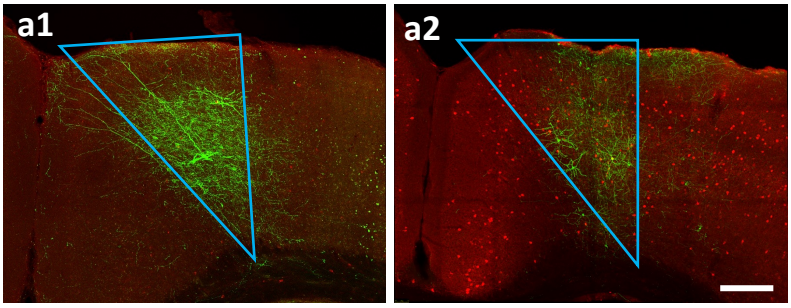

Supplementary Figure 4

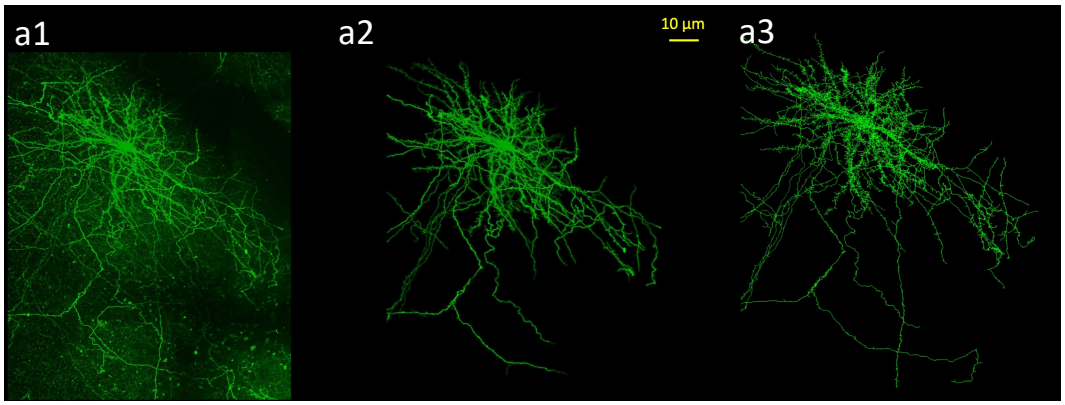

b

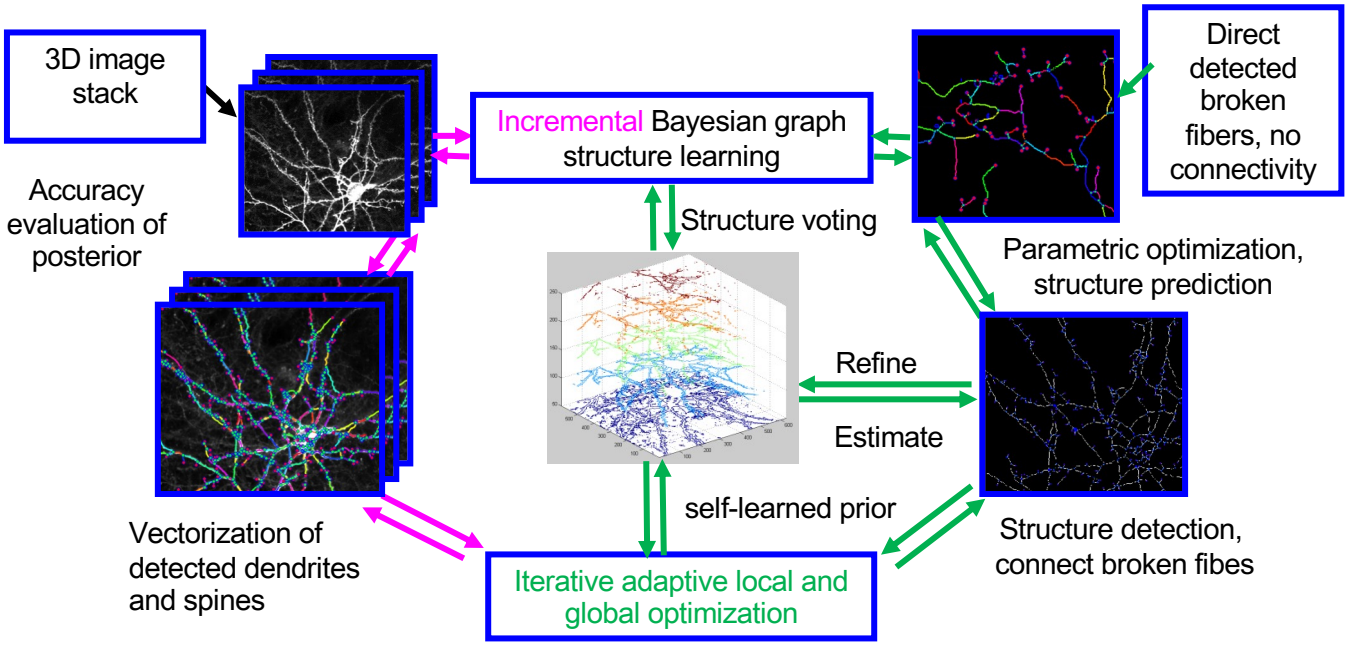
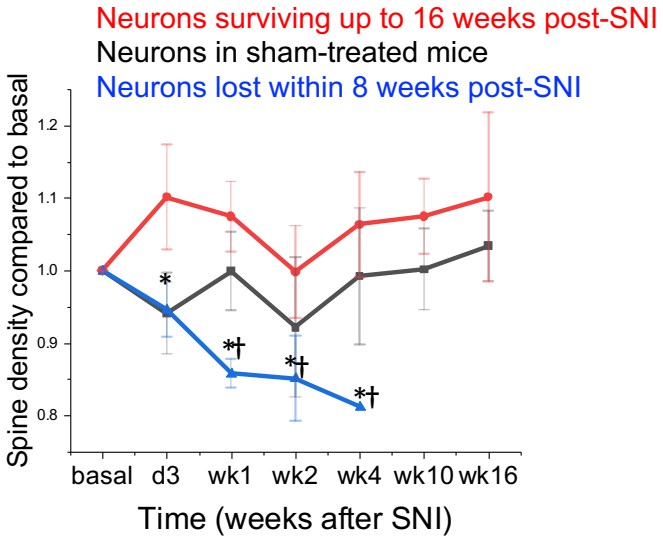
Supplementary Figure 5